Rigid ion model of high field transport in GaN

2009 J. Phys.: Condens. Matter 21 174206

(http://iopscience.iop.org/0953-8984/21/17/174206)

IOP PUBLISHING JOURNAL OF PHYSICS: CONDENSED MATTER

J. Phys.: Condens. Matter **21** (2009) 174206 (16pp) doi:10.1088/0953-8984/21/17/174206

Rigid ion model of high field transport in GaN

Shinya Yamakawa, Richard Akis, Nicolas Faralli, Marco Saraniti and Stephen M Goodnick

Department of Electrical Engineering, Arizona State University, Tempe, AZ 85287-5706, USA
and
Arizona Institute for Nanoelectronics, Arizona State University, Tempe, AZ 85287-5706, USA

E-mail: stephen.goodnick@asu.edu

Received 3 November 2008, in final form 5 February 2009
Published 1 April 2009
Online at stacks.iop.org/JPhysCM/21/174206

Abstract

Here we report on high field transport in GaN based on the rigid ion model of the electron–phonon interaction within the cellular Monte Carlo (CMC) approach. Using the rigid pseudo-ion method for the cubic zinc-blende and hexagonal wurtzite structures, the anisotropic deformation potentials are derived from the electronic structure, the atomic pseudopotential and the full phonon dispersion and eigenvectors for both acoustic and optical modes. Several different electronic structure and lattice dynamics models are compared, as well as different models for the interpolation of the atomic pseudopotentials required in the rigid pseudo-ion method. Piezoelectric as well as anisotropic polar optical phonon scattering is accounted for as well. In terms of high field transport, the peak velocity is primarily determined by deformation potential scattering described through the rigid pseudo-ion model. The calculated velocity is compared with experimental data from pulsed I–V measurements. Good agreement is found using the rigid ion model to the measured velocity–field characteristics with the inclusion of dislocation and ionized impurity scattering. The crystal orientation of the electric field is investigated, where very little difference is observed in the velocity–field characteristics. We simulate the effects of nonequilibrium hot phonons on the energy relaxation as well, using a detailed balance between emission and absorption during the simulation, and an anharmonic decay of LO phonons to acoustic phonons, as reported previously. Nonequilibrium phonons are shown to result in a significant degradation of the velocity–field characteristics for high carrier densities, such as those encountered at the AlGaN/GaN interface due to polarization effects.

(Some figures in this article are in colour only in the electronic version)

1. Introduction

The group III nitrides have received considerable attention in recent years for short wavelength optoelectronic [1] and high power, high frequency electronic applications [2]. These materials are generally wide bandgap materials and can crystallize in both wurtzite and zinc-blende polytypes, although the former is the dominant equilibrium structure [3]. Wide bandgap materials such as GaN or SiC are suitable for high temperature operation because they become intrinsic at much higher temperature than narrower bandgap materials such as Si or GaAs. The wide bandgap also results in a much higher breakdown field as the threshold field for impact ionization is much higher. The breakdown field of GaN is estimated to be above 4 MV cm^{-1}, which is much higher than Si (0.2 MV cm^{-1}) or GaAs (0.4 MV cm^{-1}). Hence they are attractive for high power applications. At the same time, the predicted high peak and saturation velocities in GaN are advantageous for high frequency operation.

GaN/AlGaN heterostructure (or high mobility) field-effect transistors (HFETs or HEMTs) have been demonstrated [4], which have shown promising performance as microwave power devices. Recent results on nanometer scale gate-length devices have demonstrated cutoff frequencies in excess of 150 GHz [5, 6]. As a result of the discontinuity of the spontaneous and piezoelectric polarization at the GaN/AlGaN interface, such structures have a high carrier density without any intentional doping of the barrier layer. Typical sheet

densities are of the order of $1–2 \times 10^{13}$ cm^{-2}, which is an order of magnitude higher than conventional AlGaAs/GaAs HFETs. While such high densities of carriers are beneficial in terms of reduced resistance and high current, the effect on transport is still little understood.

The high field transport properties of the nitrides are still relatively less well understood compared to cubic semiconductors such as Si, GaAs and InP from an experimental standpoint. Time-of-flight measurements were reported by the Army Research Laboratories in GaN p–i–n diodes, where a peak steady state velocity of 1.9×10^7 cm s^{-1} was reported [7]. Experimental studies of high field transport at Arizona State University based on pulsed I–V measurements reported peak velocities in excess of $2–3 \times 10^7$ cm s^{-1} in bulk GaN [8] and AlGaN/GaN heterostructures [9].

The ensemble Monte Carlo technique has been used now for over 30 years as a numerical method to simulate nonequilibrium transport in semiconductor materials and devices, and has been the subject of numerous books and reviews [10, 11]. The ensemble Monte Carlo algorithm consists of generating random free flight times for each particle in an representative ensemble of particles, choosing the type of scattering occurring at the end of the free flight, changing the final energy and momentum of the particle after scattering, and then repeating the procedure for the next free flight. Physical quantities of interest such as the drift velocity, average energy and distribution function are calculated as averages over the ensemble. There have been a number of ensemble Monte Carlo (EMC) simulations of transport in GaN. The first transport simulation using Monte Carlo (MC) methods was reported by Littlejohn *et al* in 1975 using a single-valley, parabolic band model [12]. In 1993, Gelmont *et al* reported a two-valley model including polar optical, deformation potential and piezoelectric phonon scattering, where intervalley electron transfer was predicted to give rise to a large negative differential conductance [13]. Mansour *et al* also used a two-valley model to simulate the high temperature dependence of the electron velocity [14]. They included acoustic phonon, polar optical phonon, intervalley phonon and ionized impurity scattering. An improved multi-valley model was reported by Bhapkar and Shur in 1997 [15]. In addition to Γ and U valleys, they included the second Γ valley (Γ2 valley) occurring in the wurtzite structure in this calculation. The energy gap between the first and second valleys was modified to 2.0 eV, which was taken from band structure calculation. The acoustic phonon, polar optical phonon, ionized impurity, piezoelectric and intervalley scattering mechanisms were considered.

All the simulations mentioned above used analytical, non-parabolic band structures. Full band EMC simulation uses the full electronic dispersion and Bloch states taken from electronic structure calculations to model the electron trajectories and scattering process, which in general provides more accurate results, particularly at high electric fields [11]. Full band MC simulations were first reported for GaN by the Georgia Tech group. Kolník *et al* reported the first full band MC simulation for both wurtzite and zinc-blende GaN [16]. Acoustic, polar optical and intervalley scattering were included in the simulation. Transport studies across a variety of wideband materials was reported by Brennan *et al* [17]. In the calculation, they used the same isotropic parameters for both zinc-blende and wurtzite GaN.

While these studies were the first full band simulations of GaN, they used electron–phonon scattering rates based on deformation potentials taken for other III–V zinc-blende materials in the absence of such information for the nitride. There have been no reported measurements of the optical and intervalley deformation potentials in the nitrides to our knowledge. Furthermore, the deformation potential scattering in general is strongly anisotropic and involves multiple phonon modes and polarizations. Hence, from a theoretical standpoint, a more complete description of high field transport from first principles should use a fully anisotropic model for electron–phonon interaction derived from the electronic structure and lattice dynamics directly.

In order to address the electron–phonon coupling from a microscopic standpoint within a full band model of electron transport, in the present paper we report on the use of the rigid pseudo-ion model (RIM) to calculate the fully anisotropic deformation potential in zinc-blende and wurtzite GaN using empirical pseudopotential band structures for both. These anisotropic rates are then used in a full band cellular Monte Carlo simulator to investigate high field transport in wurtzite GaN and compared with constant deformation potential models and available experimental data. In section 2, we first discuss the RIM approach, followed by application of this model to calculate the deformation potential limited scattering rate in cubic GaN (section 3) and hexagonal GaN (section 4). Other scattering mechanisms considered in the subsequent transport simulations are covered in section 5, followed by discussion of the cellular Monte Carlo (CMC) method and its application to high field transport in GaN using the RIM scattering rates derived earlier. The effects of nonequilibrium longitudinal optical (LO) phonons are reported as well in section 6, where a comparison of the velocity–field characteristics with and without nonequilibrium phonons is presented. Finally, we conclude in section 7.

2. Rigid pseudo-ion model

As was mentioned in section 1, the electron–phonon interaction is typically calculated by using the deformation potential in a conventional Monte Carlo (MC) simulation, with the deformation potential often adjusted to fit experimental data. Since experimental information on the deformation potentials in GaN is relatively unknown, and because of the high fields and anisotropic nature of transport in this wide bandgap system, here the deformation potential is calculated by the rigid pseudo-ion model (RIM) [18, 19].

Essentially, the rigid pseudo-ion model calculates the electron–phonon interaction potential as the effective potential associated with the rigid displacement of the atomic pseudopotentials associated with the atomic motion. The electron–phonon (non-polar) scattering rate is calculated from Fermi's golden rule as

$$P^{\eta}_{\mathrm{e-p}}(\nu, \boldsymbol{k}, \nu', \boldsymbol{k} \pm \boldsymbol{q}) = \frac{2\pi}{\hbar} |\langle \nu', \boldsymbol{k} \pm \boldsymbol{q}, N_{\eta q} \mp 1 | H_{\mathrm{e-p}} | \nu, \boldsymbol{k}, N_{\eta q} \rangle|^2 \delta(\varepsilon_{\nu', \boldsymbol{k} \pm \boldsymbol{q}} \mp \hbar\omega_{\eta q} - \varepsilon_{\nu, \boldsymbol{k}}), \quad (1)$$

where H_{e-p} is the electron–phonon interaction, $\varepsilon_{\nu,\boldsymbol{k}}$ and $\varepsilon_{\nu',\boldsymbol{k}\pm\boldsymbol{q}}$ are the electron energies before and after scattering, respectively, and ν' denotes the band after scattering. The upper and lower signs correspond to absorption and emission of a phonon, respectively, and the phonon occupation number, $N_{\eta\boldsymbol{q}}$, is given by the Bose–Einstein distribution function.

The Hamiltonian for the electron–phonon interaction is derived from the electron–ion potential. In general, we need to sum the potential change for all the atoms in the crystal. The potential change due to the atomic displacement is (assuming small displacements)

$$\begin{aligned} H_{e-p} &= \sum_{l,\kappa}[V_\kappa(\boldsymbol{r}-\boldsymbol{R}_{l,\kappa}+\boldsymbol{u}_{l,\kappa})-V_\kappa(\boldsymbol{r}-\boldsymbol{R}_{l,\kappa})] \\ &= \sum_{l,\kappa}\boldsymbol{u}_{l,\kappa}\,\mathrm{grad}V_\kappa(\boldsymbol{r}-\boldsymbol{R}_{l,\kappa}), \end{aligned} \tag{2}$$

where $\boldsymbol{R}_{l,\kappa}$ is the equilibrium position of the κth atom in the lth unit cell and $\boldsymbol{u}_{l,\kappa}$ is its displacement from equilibrium, which is represented by the Fourier expansion over $\boldsymbol{q}$:

$$\boldsymbol{u}_{lk}^{(\eta)} = \sum_{\boldsymbol{q}}\sqrt{\frac{\hbar}{2M_\kappa N\omega_{\eta\boldsymbol{q}}}}(a_{\boldsymbol{q}}+a_{-\boldsymbol{q}}^{\dagger})\boldsymbol{e}_\kappa^{(\eta)}(\boldsymbol{q})\,\mathrm{e}^{\mathrm{i}\boldsymbol{q}\cdot\boldsymbol{R}_{l\kappa}}, \tag{3}$$

where M_κ is the atomic mass, N is the number of primitive cells and $\boldsymbol{e}_\kappa^{(\eta)}(\boldsymbol{q})$ denotes the normalized polarization vector of phonons of branch η for the atom type κ. Let $\boldsymbol{R}_{l,\kappa}=\boldsymbol{R}_l+\boldsymbol{\tau}_\kappa$. We then obtain the relation using Bloch's theorem:

$$\begin{aligned} &\langle\nu',\boldsymbol{k}\pm\boldsymbol{q}|\mathrm{grad}V_\kappa(\boldsymbol{r}-\boldsymbol{R}_{l,\kappa})|\nu,\boldsymbol{k}\rangle \\ &= \mathrm{e}^{-\mathrm{i}\boldsymbol{q}\cdot\boldsymbol{R}_l}\langle\nu',\boldsymbol{k}\pm\boldsymbol{q}|\mathrm{grad}V_\kappa(\boldsymbol{r}-\boldsymbol{\tau}_\kappa)|\nu,\boldsymbol{k}\rangle. \end{aligned} \tag{4}$$

From equations (2) and (4), the non-zero matrix elements are

$$\begin{aligned} &\langle\nu',\boldsymbol{k}\pm\boldsymbol{q},N_{\eta\boldsymbol{q}}\mp1|H_{e-p}|\nu,\boldsymbol{k},N_{\eta\boldsymbol{q}}\rangle \\ &= \sum_\kappa\sqrt{\frac{\hbar}{2M_\kappa N\omega_{\eta\,\boldsymbol{q}}}}A_\kappa(\nu',\boldsymbol{k},\pm\boldsymbol{q},\nu)\boldsymbol{e}_\kappa^{(\eta)}(\pm\boldsymbol{q}) \\ &\quad\times\sqrt{N_{\eta\boldsymbol{q}}+\tfrac{1}{2}\mp\tfrac{1}{2}}, \end{aligned} \tag{5}$$

where

$$A_\kappa(\nu',\boldsymbol{k},\boldsymbol{q},\nu) = -\langle\nu',\boldsymbol{k}+\boldsymbol{q}|\mathrm{grad}V_\kappa(\boldsymbol{r}-\boldsymbol{\tau}_\kappa)|\nu,\boldsymbol{k}\rangle\mathrm{e}^{\mathrm{i}\boldsymbol{q}\cdot\boldsymbol{\tau}_\kappa}. \tag{6}$$

The wavefunction $|\nu,\boldsymbol{k}\rangle$ and atomic potential can be expressed by the Fourier series over the reciprocal lattice vector $\boldsymbol{G}$ (Bloch expansion):

$$|\nu,\boldsymbol{k}\rangle = \frac{1}{\sqrt{\Omega}}\sum_G C_{\nu,\boldsymbol{k}}(\boldsymbol{G})\mathrm{e}^{\mathrm{i}(\boldsymbol{k}+\boldsymbol{G})\cdot\boldsymbol{r}}, \tag{7}$$

$$V_\kappa(\boldsymbol{r}) = \tfrac{1}{2}\sum_G V_\kappa(\boldsymbol{G})\mathrm{e}^{\mathrm{i}\boldsymbol{G}\cdot\boldsymbol{r}}, \tag{8}$$

where Ω is the unit cell volume. The coefficient $V_\kappa(\boldsymbol{G})$ is expressed as

$$V_\kappa(\boldsymbol{G}) = \frac{2}{\Omega}\int_\Omega \mathrm{d}^3\boldsymbol{r}V_\kappa(\boldsymbol{r})\,\mathrm{e}^{-\mathrm{i}\boldsymbol{G}\cdot\boldsymbol{r}}. \tag{9}$$

The expansion given in equations (8) and (9) is strictly valid only if the time-varying lattice displacement is neglected since the crystal potential is not in general a periodic function due to the vibrational motion. Assuming that this time varying the component is negligible and the Bloch expansion is valid, equations (6) then become

$$\begin{aligned} A_\kappa(\nu,\boldsymbol{k},\boldsymbol{q},\nu') &= -\frac{\mathrm{i}}{2}\sum_{\boldsymbol{G},\boldsymbol{G}'}C_{\nu',\boldsymbol{k}'}^*(\boldsymbol{G}')C_{\nu,\boldsymbol{k}}(\boldsymbol{G})(\boldsymbol{G}'-\boldsymbol{G}+\boldsymbol{q}) \\ &\quad\times V_\kappa(\boldsymbol{G}'-\boldsymbol{G}+\boldsymbol{q})\cdot\mathrm{e}^{-\mathrm{i}(\boldsymbol{G}'-\boldsymbol{G})\cdot\boldsymbol{\tau}_\kappa}. \end{aligned} \tag{10}$$

Here we assume that the argument of $V_\kappa(\boldsymbol{G}'-\boldsymbol{G}+\boldsymbol{q})$ is a continuous vector in order to include the effect of lattice vibrations. This means $V_\kappa(\boldsymbol{G}'-\boldsymbol{G}+\boldsymbol{q})$ needs to be calculated by the interpolation of $V_\kappa(\boldsymbol{G})$. The deformation potential, $\Delta^{(\eta)}(\nu',\boldsymbol{k},\boldsymbol{q},\nu)$, is defined as

$$\begin{aligned} &\langle\nu',\boldsymbol{k}\pm\boldsymbol{q},N_{\eta\boldsymbol{q}}\mp1|H_{e-p}|\nu,\boldsymbol{k},N_{\eta\boldsymbol{q}}\rangle \\ &= \sqrt{\frac{\hbar}{2M_\kappa N\omega_{\eta\boldsymbol{q}}}}\Delta^{(\eta)}(\nu',\boldsymbol{k},\boldsymbol{q},\nu)\sqrt{N_{\eta\boldsymbol{q}}+\frac{1}{2}\mp\frac{1}{2}}. \end{aligned} \tag{11}$$

Comparing equations (5) and (11), the deformation potential takes the form [18]

$$\Delta^{(\eta)}(\nu',\boldsymbol{k},\boldsymbol{q},\nu) = \sqrt{M}\left|\sum_\kappa\frac{1}{\sqrt{M_\kappa}}A_\kappa(\nu',\boldsymbol{k},\boldsymbol{q},\nu)\cdot\boldsymbol{e}_\kappa^{(\eta)}(\boldsymbol{q})\right|, \tag{12}$$

where M is the sum of the atomic mass in a unit cell or $M=\sum_\kappa M_\kappa$.

The deformation potential scattering rate is calculated using Fermi's golden rule and the rigid ion approximation for the wavevector-dependent deformation potential given by equation (12). The non-polar deformation potential scattering rate from the point $\boldsymbol{k}$ in band ν to a region $\Omega_{\boldsymbol{k}'}$ in band ν' centered around the $\boldsymbol{k}'$ is written as [20]

$$\begin{aligned} P_{\nu\nu',\eta}^{\mathrm{def}}(\boldsymbol{k},\Omega_{\boldsymbol{k}\pm\boldsymbol{q}}) &= \frac{\pi}{\rho\omega_{\eta\boldsymbol{q}}}|\Delta^{(\eta)}(\nu',\boldsymbol{k},\boldsymbol{q},\nu)|^2 \\ &\quad\times|I(\nu,\nu';\boldsymbol{k},\boldsymbol{k}\pm\boldsymbol{q})|^2D_{\nu'}(E',\Omega_{\boldsymbol{k}'})(N_{\eta\boldsymbol{q}}+\tfrac{1}{2}\mp\tfrac{1}{2}), \end{aligned} \tag{13}$$

where ρ is the semiconductor density, $I(\nu,\nu';\boldsymbol{k},\boldsymbol{k}\pm\boldsymbol{q})$ is the overlap integral between initial and final Bloch states and $D_{\nu'}(E',\Omega_{\boldsymbol{k}'})$ is the density of states in $\Omega_{\boldsymbol{k}'}$ at energy $E'=E(\boldsymbol{k})\pm\hbar\omega_{\eta\boldsymbol{q}}$. As can be seen from this derivation, calculation of the anisotropic deformation potential requires the eigenstates and eigenvectors of both the electronic structure and lattice dynamics, as well as a model for the wavevector-dependent atomic pseudopotentials, as discussed next.

3. Rigid ion model for zinc-blende GaN

3.1. Empirical pseudopotential method (EPM) band structure

There are various approaches to the calculation of electronic structure ranging from *ab initio* (e.g. density functional theory) to empirical. While work is on-going to incorporate fully *ab initio* electronic structure and scattering rates into transport simulation, for the rigid ion calculation and full band EMC simulations discussed in the present paper, we have used the empirical pseudopotential method (EPM) for the electronic band structure of both zinc-blende and wurtzite GaN, which uses empirically derived form factors to represent the electronic pseudopotential at various reciprocal lattice vectors, $\boldsymbol{G}$ [21]. For zinc-blende GaN, we have compared

the results of using two different zinc-blende EPM calculations reported in the literature, those due to Oğuzman *et al* [22] and a second set due to Xia *et al* [23]. While Oğuzman *et al* fit the symmetric and antisymmetric components of the lattice potential, V_s and V_a, at specific reciprocal lattice points, Xia *et al* fit the *atomic* pseudopotentials of Ga and N to a functional form suggested by Schlüter *et al* [24]:

$$V_\alpha(\boldsymbol{G}) = a_1(G^2 - a_2)/[1 + \exp(a_3(G^2 - a_4))]. \qquad (14)$$

Figure 1(a) shows the comparison of the two band structures, which are quite similar for the Γ valley, but show differences at higher energies. In the present work, 113 reciprocal lattice vectors were used in the calculation.

A key quantity related to electron–phonon scattering rates is the electronic density of states (DOS):

$$\rho(E) = \sum_\nu \int \mathrm{d}^3\boldsymbol{k}\, \delta(E_\nu(\mathbf{k}) - E), \qquad (15)$$

where $E_\nu(\boldsymbol{k})$ is the energy for electrons with band index ν and wavevector $\boldsymbol{k}$. Exploiting the symmetries of the zinc-blende structure, the region over which the integration need actually be done can be reduced to the 1/48 irreducible reference wedge in the first Brillouin zone (BZ), which is illustrated in the inset of figure 1(b) and defined by the inequalities

$$k_x + k_y + k_z \leqslant \frac{3}{2}\left(\frac{2\pi}{a}\right), \qquad k_z \leqslant k_x \leqslant k_y. \qquad (16)$$

To obtain the DOS numerically, we first compute the energy levels corresponding to conduction band index ν, $E_\nu(\boldsymbol{k}_\lambda)$ at discrete points, $\boldsymbol{k}_\lambda, \lambda = 1, \ldots, 916$, in the wedge. These points are chosen to be equally spaced, separated by $0.05(2\pi/a)$ along each direction, and only the first five conduction bands are used. For the actual integration, we use the quadratic interpolation algorithm developed by Wiesenekker and Baerends [25]. Figure 1(b) shows the DOS for zinc-blende GaN using the two different models. Note that, in either case, after the initial increase the DOS shows considerable structure, much of which falls below the initial peak. In contrast, a simple non-parabolic model would be monotonically increasing.

While the EPM calculation for the band structure involves pseudopotential form factors defined at discrete reciprocal lattice vectors, the RIM calculation for the electron–phonon scattering rate given by equation (12) requires the atomic pseudopotentials, $V_\alpha(q)$, at *arbitrary values of* q. Unfortunately the interpolation of the atomic pseudopotentials has been a matter of some controversy: hence we have considered more than one approach. The first was to take the form factors of Oğuzman *et al* [22] and use cubic splines to interpolate between the values set at the reciprocal lattice vector points. The results of this interpolation are shown in figure 2(a). As part of this interpolation scheme, we included the additional constraint that $V_\alpha(q = 0) = 0$. On the surface, this constraint would appear to be arbitrary and unphysical, as $V_\alpha(0)$ should represent the average value of the potential in the unit cell according to Fourier analysis.

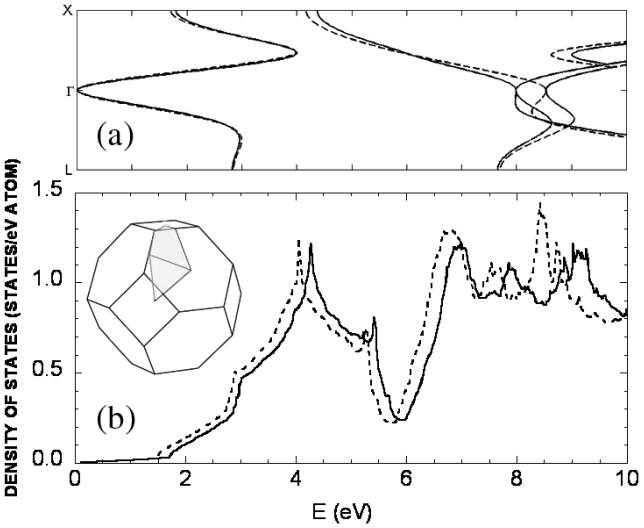

Figure 1. (a) The electronic band structure of zinc-blende GaN, generated using the pseudopotential form factors of Oğuzman *et al* (solid line) and those of Xia *et al* (dashed). (b) The electronic density of states as a function of energy using the Oğuzman *et al* (solid line) and Xia *et al* (dashed line) pseudopotential form factors. Inset: an irreducible reference wedge in the first Brillouin zone.

However, this assumption is mitigated by the fact that the truly significant quantity as far as the matrix elements are concerned is $qV_\alpha(q)$, which will go to zero at $q = 0$. Moreover, it has been argued that applying this assumption in the case of Si give more consistent results for full-band Monte Carlo simulations [26]. The reason for this appears to be that the $V_\alpha(q = 0) = 0$ constraint tends to limit the size of the oscillations in $V_\alpha(q)$ in the region of small q. Removing the constraint and allowing $V_\alpha(q)$ to 'float' freely tends to result in $V_\alpha(q)$ taking on very large magnitude values in this region. This has been illustrated for the example of Si in a comment by Bednarek and Rössler [25]. Another approach with regards to interpolation is to assume that $V_\alpha(q)$ follows a particular functional form, which naturally brings us back to equation (14). In figure 2(b) the atomic form factors for Ga and N are plotted using equation (14) and the parameters reported by Xia *et al*.

3.2. Phonon spectra

To calculate the phonon dispersion, we have used the valence-shell model [26, 27], which uses ten adjustable parameters to generate the required dynamical matrices, and was modified to fit the phonon dispersion curves of zinc-blende lattice structures. One complication is that, before obtaining the dispersion, one needs sufficient phonon data in order to fit the parameters. Unfortunately, as mentioned in section 1, very few GaN phonon frequencies have actually been determined experimentally, a problem even more acute for the zinc-blende phase. As such, we have used the results from some earlier theoretical calculations of phonon spectra to perform the shell model fitting. In figure 3(a), we plot the phonon dispersion along lines of symmetry using the best shell model fit obtained using points experimentally determined by Azuhata

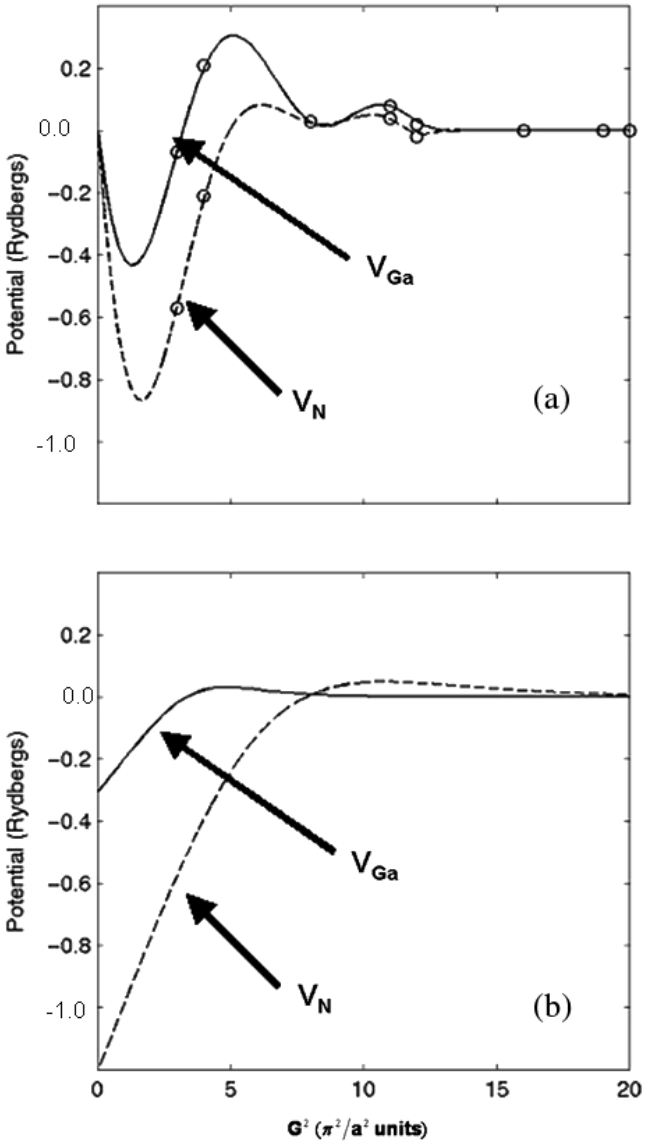

Figure 2. (a) The ionic pseudopotentials of Ga and N as a function of the square of the magnitude of reciprocal lattice vectors. The circles are the form factors reported by Oğuzman *et al*. The lines represent a cubic-spline fit with the constraint that $V_\alpha(q = 0) = 0$. (b) As in (a), except that the curves are given by equation (14) using Xia *et al*'s parameters.

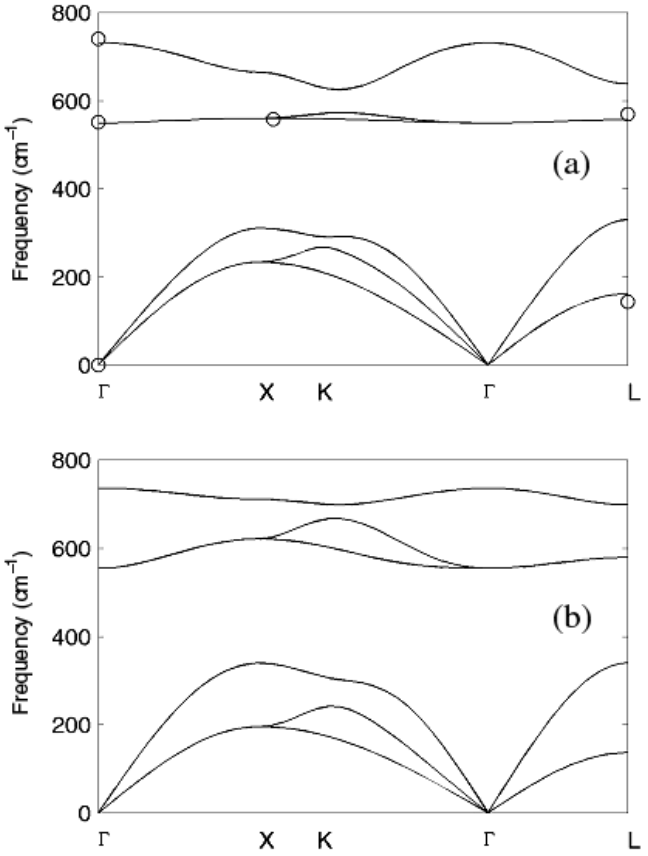

Figure 3. The calculated phonon dispersion of GaN along high symmetry lines obtained from a valence-shell model calculation fit to the data of Zi *et al* and Azuhata *et al* (a) and Karch *et al* (b).

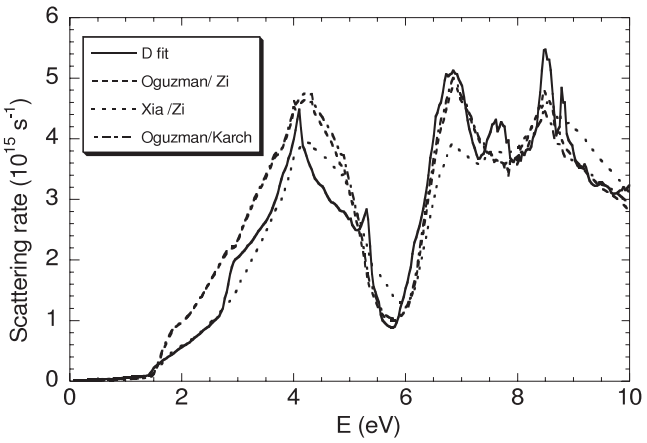

Figure 4. Electron–phonon scattering rate versus energy for the three cases discussed in the text. The solid line represents the product of the DOS with a fitted optical deformation potential.

et al [28] (circles) as well as data extracted from dispersion curves calculated theoretically by Zi *et al* using the Keating model [29]. Figure 3(b) shows the results obtained using shell model fits to data points extracted from the dispersion curves calculated by Karch *et al* within the framework of self-consistent density functional perturbation theory [30]. There are obvious differences, such as the relative lack of dispersion of the TO branches of the Zi *et al* fit compared to the fit to Karch *et al*. The frequencies attained by the TA branches tend to be significantly higher in the latter case as well.

3.3. Calculated scattering rate

The anisotropic scattering rate given by equation (13) may be averaged over all final states and phonon modes to realize an energy-dependent scattering rate. In figure 4 we show the electron–phonon scattering rate for three different cases. The dashed curve is obtained using Oğuzman *et al*'s pseudopotentials and the fit to Zi *et al*'s phonon dispersion curves. For the dotted curve, the fit to the Zi *et al* dispersion was used, but Xia's form factors were used for the pseudopotentials. Finally, for the

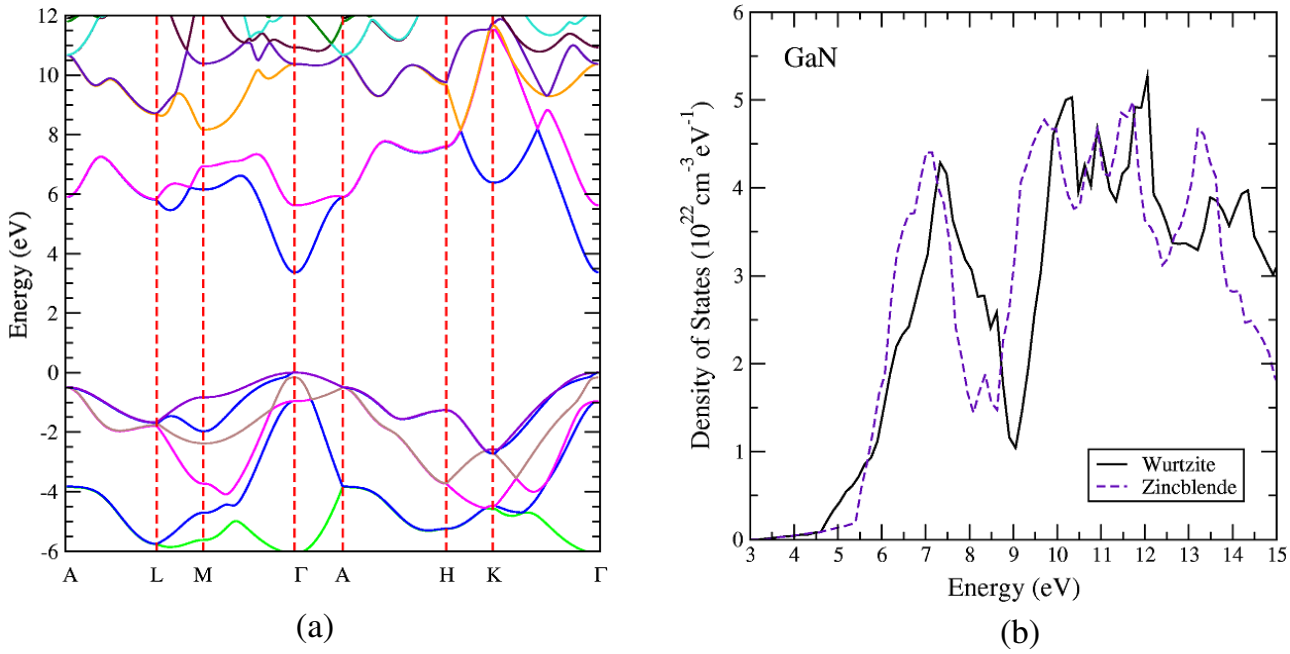

Figure 5. EPM band structure of wurtzite GaN used in the present work and the corresponding density of states comparing wurtzite GaN to a similar EPM calculation of the cubic zinc-blende phase.

dashed–dotted curve, Oğuzman *et al*'s pseudopotentials are again used, while the phonon dispersion used in this case is the shell model fit to Karch *et al*. Comparing the results, it is evident that for the particular cases we considered, there was a greater sensitivity to the model used for the phonon dispersion than for the choice of the pseudopotentials. That said, one can observe that the overall sensitivity to the EPM calculation and phonon dispersion is relatively small overall, which provides a satisfactory degree of confidence in the overall method.

Given the energy-dependent scattering rate shown in figure 4, it is also useful to connect to the usual deformation potential approximation of scattering, for which it is assumed that the deformation potentials are energy-and wavevector-independent. The main energy dependence then enters through the DOS, where the optical deformation potential electron–phonon scattering rate can be written as

$$\frac{1}{\tau_{\text{el-ph}}(E)} \propto D^2 \rho(E') \tag{17}$$

where D is an optical deformation potential with units of eV cm^{-1} and $\rho(E')$ is the density of final states (initial plus or minus the phonon energy).

Using a least-squares fit, we have extracted D from equation (17), the calculated DOS from the band structure of Oğuzman *et al* and the corresponding scattering rate of Oğuzman/Zi in figure 4. In figure 4, the solid line is the result obtained using a fitted value of $D = 1.32 \times 10^9$ eV cm^{-1}. As can be seen, the overall fit is relatively good. It should be noted that, in using equation (17), we assume a single optical phonon frequency of 280 cm^{-1}, or 35 meV, which corresponds to the LA frequency at the X point.

4. Rigid ion model for wurtzite GaN

4.1. EPM band structure

While GaN may exist in either the cubic zinc-blende structure or the hexagonal wurtzite structure, the dominant crystal phase encountered in electronic and optoelectronic materials is the hexagonal phase. For the wurtzite band structure, we use the pseudopotential form factors for wurtzite reported by Oğuzman *et al* [22] in previous full band Monte Carlo studies, where 183 plane waves, corresponding to different reciprocal lattice vectors, are used for the wurtzite lattice. Here, reciprocal vectors up to the twentieth nearest neighbors are used for the wurtzite lattice. In the band calculation of the wurtzite lattice, the conduction bands are shifted by −0.92 eV in order to fit the result to the experimental values for the gap (3.4 eV) as discussed by Kolník [16]. This shift is necessary because the band structure was extracted to fitting the effective mass rather than the bandgap, since the correct conduction band effective mass is more important with respect to electronic transport. The calculated band structure is shown in figure 5. As can be seen, the second valley for wurtzite GaN is at the middle point (U) between the L and M points, where the energy is 2.0 eV above the conduction band minimum. The density of states (DOS) obtained from this band structure is also shown in figure 5, compared with the corresponding DOS for zinc-blende GaN (no longer normalized per atom).

As discussed in detail in sections 2 and 3, the electron–phonon scattering rate involves both the eigenvalues and eigenvectors of the electronic motion, e.g. the Bloch states calculated from EPM, as well as the phonon eigenvalues and eigenvectors. Further, the dependence of $V_\alpha(\boldsymbol{q})$ on $\boldsymbol{q}$ requires the representation of the atomic potential over a continuous range of wavevectors rather than at discrete points in $\boldsymbol{k}$

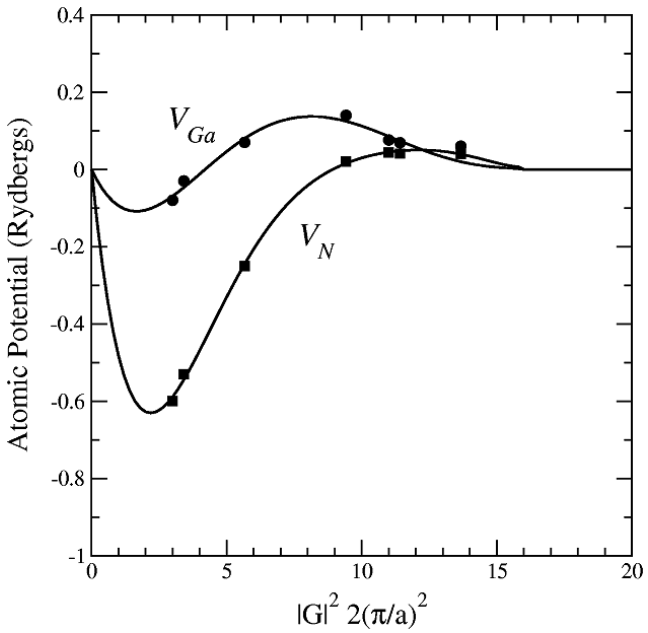

Figure 6. EPM pseudopotential for wurtzite Ga and N as a function of the squared magnitude of reciprocal lattice vector $\boldsymbol{G}$ (here treated as a continuous function). The circle and square points are the pseudopotentials of Ga and N atoms, respectively.

corresponding to specific reciprocal lattice vectors. Here we again use the approach suggested by Fischetti *et al* [31], in which a polynomial fit is used for the atomic potentials, which are extrapolated to zero for small $\boldsymbol{q}$. The interpolated form factors for Ga and N are shown in figure 6.

4.2. Phonon spectra

In order to determine the sensitivity of the electron–phonon scattering rate to the lattice dynamics model used, as was done for zinc-blende GaN in section 3, we have also performed a semi-empirical calculation of the phonon spectra in wurtzite GaN using both the Keating potential method and the valence force model (VFM). Little difference was found in the charge transport properties using the two methods, similar to the results discussed in section 6. Because of the lower symmetry of the wurtzite structure, a more sophisticated lattice dynamics model is required. Here a modified VFM reported by Siegle *et al* [32] was used in the present work. This model uses five valence force potentials and one effective charge amount for the Coulomb term. The valence force potentials are used for the bond-stretching, bond-bending and MSBN interaction [33], which is the bond-bending force between three adjacent lattice bonds. The anisotropic effect of wurtzite GaN is taken into account by two sets of parameters: one representing the interaction along the c axis and the other perpendicular to it. We then fit the phonon dispersion to the experimental data [34] by least-squares fitting, using the various valence force potentials as parameters. Figure 7 shows the calculated Keating and VFM phonon dispersion for wurtzite GaN compared with experiment [34]. Due to the reduced symmetry and larger number of atoms per unit cell (4), there are more optical modes compared to the zinc-blende spectra shown in figure 3. Due to the anisotropy of the crystal, the longitudinal optical (LO) phonon branch is discontinuous with slightly different frequencies at the zone center for modes propagating in the basal plane of the hexagonal lattice (E_1(LO)) versus those perpendicular (A_1(LO)). In addition to new optical branches between the TO and LO frequencies, there are the equivalent of folded modes of the zinc-blende structure that have non-zero frequencies at the zone center (E_2^1 and B_1^1).

4.3. Anisotropic deformation potential and calculated scattering rates

From equation (12), the anisotropic (i.e. $\boldsymbol{q}$-dependent) deformation potential may be calculated within the RIM.

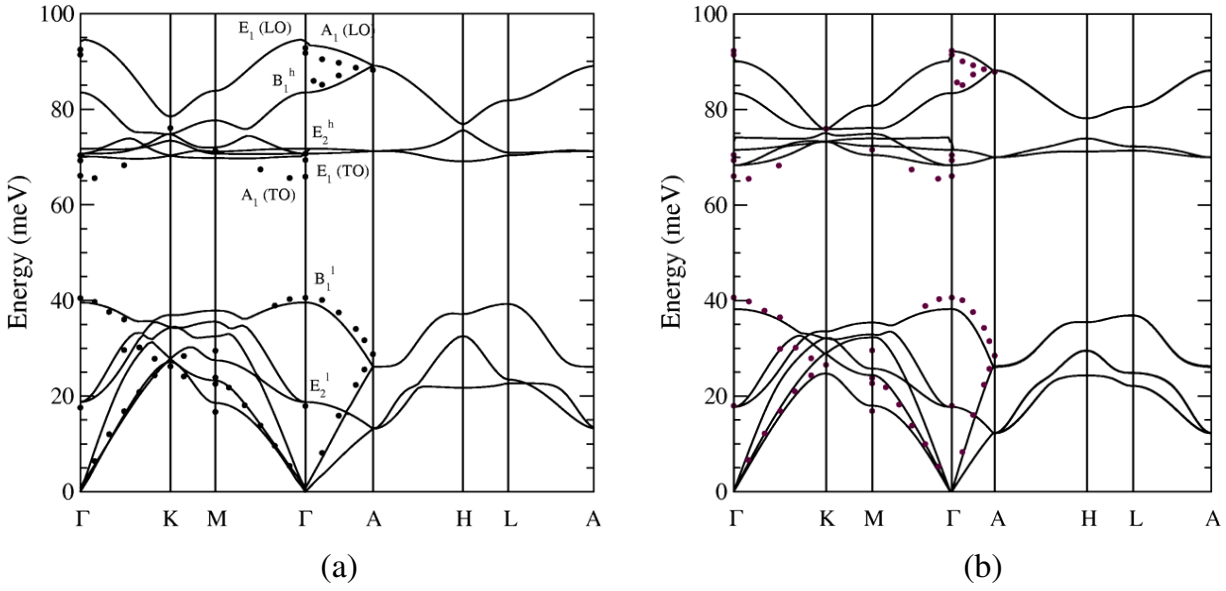

Figure 7. Phonon dispersion for wurtzite GaN by (a) Keating model (solid curves) and (b) valence force model (solid curves). The experimental data of Ruf *et al* [34] is shown by the symbols.

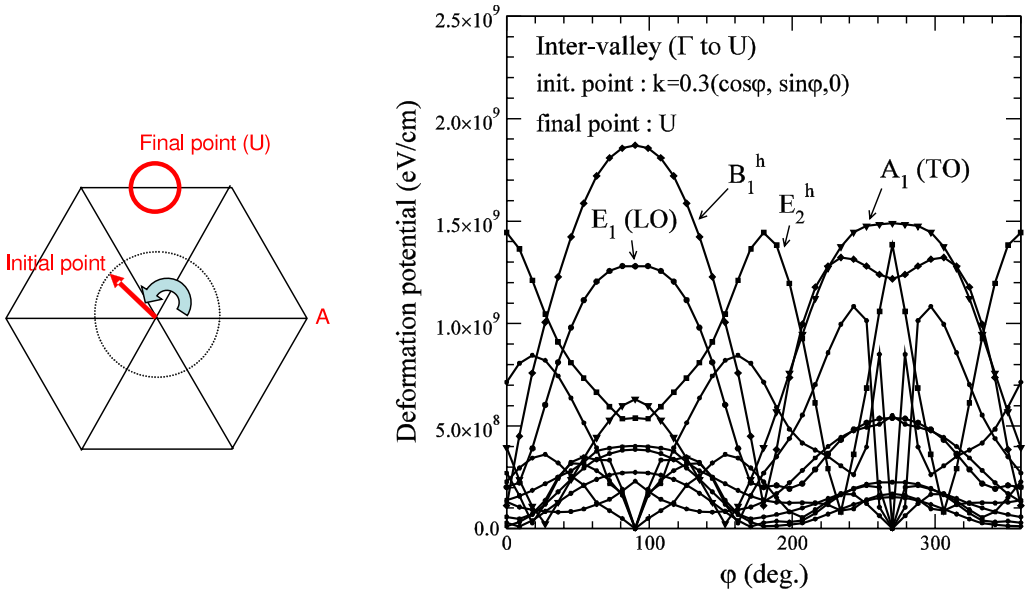

Figure 8. Intervalley deformation potentials from Γ to U in wurtzite GaN for the various phonon modes shown in figure 7. The initial point is moved around the Γ point as $\boldsymbol{k} = 0.3(\cos\varphi, \sin\varphi, 0)$, which conserves energy. The k-vector unit is $(4\pi/3a)$. The angle is measured from point A in the figure.

Figure 8 shows a typical angular dependence of the calculated deformation potential for a counterclockwise rotation of the initial wavevector for a fixed final state at point U (upper valley minimum) in the Brillouin zone. For this particular case, the longitudinal optical modes tend to dominate the scattering rate, although TO play a role as well. As is evident from this plot, the deformation potential for any given phonon mode is highly anisotropic and strongly dependent on the mode and wavevector.

By taking the momentum average of the anisotropic scattering rates at each energy, a comparative plot of the deformation potential scattering rate versus energy can be obtained, as shown in figure 9. Here we compare two different phonon models, the VFM discussed earlier and the Keating potential model. Also shown is the rate calculated using an isotropic deformation potential, as used in previous full band calculations for GaN. Four conduction bands are included in the scattering rate calculation. The deformation potentials obtained by the rigid pseudo-ion model are used only for the first and second conduction bands in order to reduce the computational resources needed. Constant deformation potentials (10.1 eV for the acoustic deformation potential scattering and 13.2×10^8 eV cm^{-1} for the non-polar optical deformation potential scattering based on the value extracted for zinc-blende in section 3) are used for the third and fourth conduction bands. The deformation potential scattering rate using the rigid pseudo-ion model is shown in figure 9, where the rate is averaged over constant energy surfaces (solid line). The solid line is the deformation potential scattering rate with the phonon dispersion using the Keating model. The dashed–dotted line is the deformation potential scattering rate using constant deformation potentials. The same constant deformation potentials mentioned above are used for all four conduction bands. The scattering rate for the rigid pseudo-ion

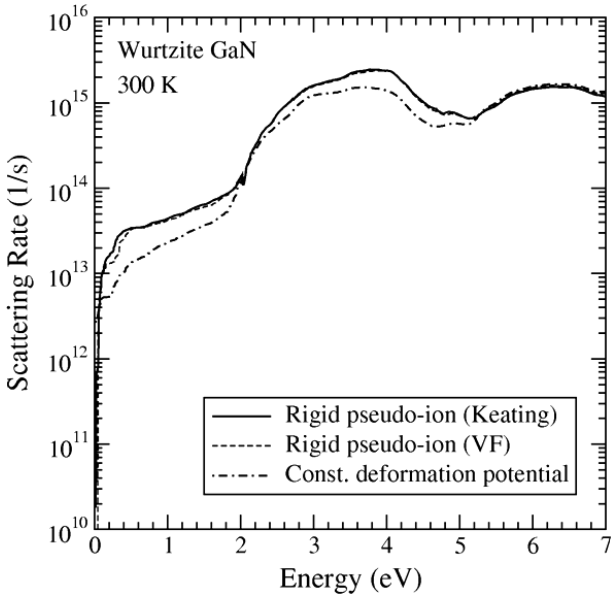

Figure 9. Deformation potential scattering rate using rigid pseudo-ion model. The solid line is the deformation potential scattering rate with the phonon dispersion using the Keating model. The dashed line is the rate using the valence force (VF) model. The dashed–dotted line is the rate using constant deformation potentials.

model is higher than by the conventional constant parameter deformation potential, which strongly affects the electron transport, as discussed in section 5. In order to check the effect of the phonon dispersion difference, the scattering rate with the phonon using the valence force (VF) model is also shown in the picture (dashed line). As is clearly seen, the scattering rate with the valence force is almost the same as the one with the Keating model. In contrast, the constant deformation potential

Table 1. Parameters for polar optical phonon scattering. The phonon energies are from [35].

$\hbar\omega_z$	66.08 (meV)	ε_z^0	12.2
$\hbar\omega_{z\mathrm{L}}$	91.13 (meV)	ε_z^∞	5.8
$\hbar\omega_\perp$	69.55 (meV)	$\varepsilon_\perp^0$	9.5
$\hbar\omega_{\perp L}$	92.12 (meV)	$\varepsilon_\perp^\infty$	5.35

Table 2. Parameters for piezoelectric scattering [39].

e_{15}	e_{31}	e_{33}	C_L (Pa)	C_T (Pa)
−0.3	−0.33	0.65	2.65×10^{11}	4.42×10^{10}

model shows significant differences, at low and medium energy ranges, which ultimately affect high field transport.

5. Other scattering mechanisms

5.1. Anisotropic polar optical phonon scattering

Polar optical phonon scattering is the dominant scattering mechanism for compound semiconductors like GaAs or GaN at room temperature for low electric fields, at least in low doped materials with good crystal quality. In general, the electron–phonon coupling in zinc-blende crystals is due to a single longitudinal optical (LO) mode phonon. In wurtzite GaN, however, the coupling is different, including in longitudinal optical (LO)-like and transverse optical (TO)-like modes [35], since these phonon modes in wurtzite crystals are neither purely longitudinal or transverse (the [0001] direction excepted) [36]. Here, both the LO-like and the TO-like mode polar optical phonon scattering rates are calculated. As discussed in [35], the scattering rate is calculated based on Fermi's golden rule:

$$P^{\mathrm{pol}}_{\nu\nu',\eta}(\boldsymbol{k}, \Omega_{\boldsymbol{k}\pm\boldsymbol{q}}) = \frac{2\pi}{\hbar}|C^{(\eta)}(\boldsymbol{q})|^2 |I(\nu, \nu'; \boldsymbol{k}, \boldsymbol{k}\pm\boldsymbol{q})|^2 \times D_{\nu'}(E', \Omega_{\boldsymbol{k}'})(N_{\eta\boldsymbol{q}} + \tfrac{1}{2} \mp \tfrac{1}{2}) \tag{18}$$

where $I(\nu, \nu'; \boldsymbol{k}, \boldsymbol{k} \pm \boldsymbol{q})$ is the Bloch overlap factor and $D_{\nu'}(E', \Omega_{\boldsymbol{k}'})$ is the density of states as before. $C^{(\eta)}(\boldsymbol{q})$ is the electron–phonon coupling coefficient. Since the wurtzite structure is a uniaxial crystal, the electron–phonon coupling coefficient is formally different from the well-known Fröhlich expression and couples the interaction associated with purely longitudinal modes in cubic structures, with the transverse optical modes. The coupling coefficients for the anisotropic uniaxial crystal have been reported by Lee *et al* [36], in which $C^{(\eta)}(\boldsymbol{q})$ may be broken into longitudinal and transverse optical phonon components, expressed as

$$C^{\mathrm{LO-like}}(\boldsymbol{q}) = \frac{2\pi e^2\hbar}{Vq^2\omega_q^{\mathrm{LO}}}\left[\frac{\sin^2\theta_q}{(1/\varepsilon_\perp^\infty - 1/\varepsilon_\perp^0)\omega_{\perp\mathrm{L}}^2} + \frac{\cos^2\theta_q}{(1/\varepsilon_z^\infty - 1/\varepsilon_z^0)\omega_{z\mathrm{L}}^2}\right] \tag{19}$$

$$C^{\mathrm{TO-like}}(\boldsymbol{q}) = \frac{2\pi e^2\hbar}{Vq^2\omega_q^{\mathrm{TO}}} \times \frac{(\omega_{\perp\mathrm{T}}^2 - \omega_{z\mathrm{T}}^2)^2 \sin^2\theta_q \cos^2\theta_q}{(\varepsilon_\perp^0 - \varepsilon_\perp^\infty)\omega_{\perp\mathrm{T}}^2\cos^2\theta_q + (\varepsilon_z^0 - \varepsilon_z^\infty)\omega_{z\mathrm{T}}^2\sin^2\theta_q} \tag{20}$$

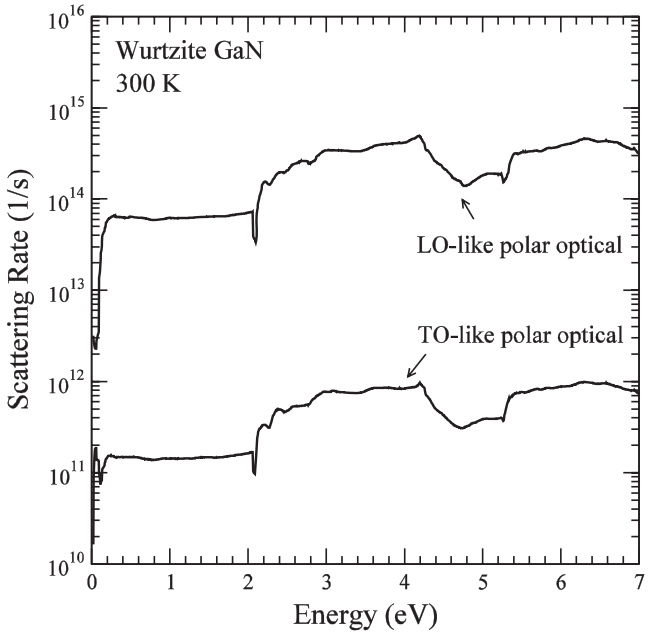

Figure 10. Polar optical phonon scattering rate in wurtzite GaN.

where θ_q is the angle between the [0001] direction (c axis) and the phonon vector $\boldsymbol{q}$, V is the crystal volume, $\omega_q^{\mathrm{LO}}(\omega_q^{\mathrm{TO}})$ is the LO-like (TO-like) mode phonon frequency, $\omega_{\perp\mathrm{T}}(\omega_{z\mathrm{T}})$ is the TO mode phonon frequency perpendicular to (along) the c axis at the zone center and $\omega_{\perp L}(\omega_{z\mathrm{L}})$ is the LO mode phonon frequency perpendicular to (along) the c axis at the zone center. ε^∞ is the high frequency dielectric constant and ε^0 is the static dielectric constant, where the subscript $\perp$ denotes perpendicular to (along) the c axis. The parameters used in this work are listed in table 1.

Figure 10 shows the calculated polar optical phonon scattering rate in wurtzite GaN based on equations (18)–(20). The LO-like polar optical phonon scattering rate is more than two orders of magnitude stronger than the TO-like mode polar optical phonon scattering. Hence, the LO-like mode phonon dominates the polar optical electron–phonon interaction in the wurtzite GaN. In this work, both polar optical scattering modes are employed.

5.2. Piezoelectric scattering

In crystals which lack inversion symmetry, elastic strain due to acoustic phonons may be accompanied by a microscopic electric field, which leads to piezoelectric scattering. The piezoelectric effect is known to be strong in nitride materials. Thus, the consideration of piezoelectric scattering effects for electron transport in GaN is important. The matrix element for piezoelectric scattering is given by the following equation [37]:

$$\langle \boldsymbol{k}'|V_{\mathrm{pz}}(\boldsymbol{k}' - \boldsymbol{k})|\boldsymbol{k}\rangle = \begin{cases} C_{\mathrm{pz}}(\boldsymbol{q})\sqrt{N_q} \\ C_{\mathrm{pz}}^\dagger(\boldsymbol{q})\sqrt{N_q + 1} \end{cases} \tag{21}$$

$C_{\mathrm{pz}}(\boldsymbol{q})$ is expressed as

$$C_{\mathrm{pz}}(\boldsymbol{q}) = \frac{ee_{\mathrm{pz}}^*}{\varepsilon^*}\sqrt{\frac{\hbar}{2MN\omega_q}} \tag{22}$$

where e^*_{pz} and ε^* are the effective piezoelectric constant, and effective dielectric constant, respectively. For simplicity, the equipartition approximation is used and the square of the matrix element becomes

$$|\langle \boldsymbol{k}'|V_{pz}(\boldsymbol{k}'-\boldsymbol{k})|\boldsymbol{k}\rangle|^2 = \frac{e^{*2}_{pz}}{\varepsilon^{*2}}\frac{e^2\hbar}{2MN\omega_q^{LA}}\frac{k_BT}{\hbar v_s q} = \frac{e^{*2}_{pz}}{\rho v_s \varepsilon^*}\frac{e^2 k_BT}{2L^3q^2\varepsilon^*} = K^2_{av}\frac{e^2k_BT}{2L^3q^2\varepsilon^*}, \quad (23)$$

where v_s is the sound velocity, ρ is the density, ω_q^{LA} is the LA mode phonon frequency and L^3 is the lattice volume. K_{av} is called the electromechanical coupling coefficient. For zinc-blende crystals, K_{av} is expressed in the following form [38]:

$$K^2_{av} = \frac{e^2_{14}}{\varepsilon}\left(\frac{12}{35c_L}+\frac{16}{35c_T}\right) \quad (24)$$

where

$$c_L = c_{12}+2c_{44}+\tfrac{3}{5}c^*, \qquad c_T = c_{44}+\tfrac{1}{5}c^*, \qquad c^* = c_{11}-c_{12}-2c_{44}. \quad (25)$$

e_{14} is the piezoelectric constant in the zinc-blende crystal and c_{11}, c_{12}, c_{44} are elastic constants. For the wurtzite lattice, the K_{av} becomes [38]

$$K^2_{av} = \frac{\langle e_l^2\rangle}{\varepsilon^* c_L}+\frac{\langle e_t^2\rangle}{\varepsilon^* c_T} \quad (26)$$

where

$$\langle e_l^2\rangle = \tfrac{1}{7}e^2_{33}+\tfrac{4}{35}e_{33}(e_{31}+2e_{15})+\tfrac{8}{105}(e_{31}+2e_{15})^2,$$
$$\langle e_t^2\rangle = \tfrac{2}{35}(e_{33}-e_{31}-e_{15})^2+\tfrac{16}{105}e_{15}(e_{33}-e_{31}-e_{15}) + \tfrac{16}{35}e^2_{15}. \quad (27)$$

The parameters are listed in table 2. The scattering rate is then written as

$$P^{piezo}_{\nu\nu'}(\boldsymbol{k},\Omega_{\boldsymbol{k}'}) = \frac{2\pi}{\hbar}K^2_{av}\frac{e^2k_BT}{q^2\varepsilon^*}|I(\nu,\nu';\boldsymbol{k},\boldsymbol{k}')|^2 D_{\nu'}(E',\Omega_{\boldsymbol{k}'}) \quad (28)$$

which includes both absorption and emission processes.

5.3. Dislocation and ionized impurity scattering

Due to the lack of a lattice-matched substrate for nitride growth, the typical density of dislocations is of the order of 10^9–10^{11} cm^{-2}, which is much higher than in conventional GaAs-based LEDs or lasers. In GaAs-based devices, a dislocation density of 10^4 cm^{-2} is sufficient to suppress lasing, for example. The fact that GaN LEDs show good performance with much higher dislocation densities, indicates that dislocations in GaN may not form trap states within the bandgap. Several experimental investigations indicate that dislocations may be charged and show acceptor-like behavior. This fact is also confirmed by the recent scanning capacitance microscopy imaging of threading dislocations, which indicates acceptor-like traps [40, 41]. Bonch-Bruevich *et al* [42] calculated the potential due to vertical line charges and Pödör obtained a momentum relaxation rate and mobility after averaging over energy [43]. Weimann *et al* [44] employed this relaxation rate and obtained good agreement with measured Hall mobility in wurtzite GaN. The same approach by Weimann *et al* is used in this work.

The screened potential energy at a large distance from a charged dislocation can be expressed using a zero-order modified Bessel function:

$$U(r) = \frac{1}{4\pi\varepsilon}\frac{2ef}{c}K_0\left(\frac{r}{\lambda}\right) \quad (29)$$

where c is the lattice parameter along the (0001) direction, f is the fraction of filled traps ranging from 0 to 1, and λ is the Debye length:

$$\lambda = \sqrt{\frac{\varepsilon k_BT}{e^2n}} \quad (30)$$

where n is the free carrier concentration. The scattering due to dislocation line charges is essentially two-dimensional, because only carriers moving perpendicular to the line charges are scattered. The Fourier transform of the scattering potential is obtained by the two-dimensional integration:

$$A(\boldsymbol{q}) = \int_0^\infty\int_0^{2\pi}\frac{e^2\lambda^2}{2\pi\varepsilon c}K_0(x)e^{-iq\lambda x\cos\theta}x\,d\theta\,dx \quad (31)$$

where $x = r/\lambda$, $\boldsymbol{q} = \boldsymbol{k}'_\perp - \boldsymbol{k}_\perp$, $\boldsymbol{k}_\perp$ is the incoming wavevector and $\boldsymbol{k}'_\perp$ is the outgoing. Look *et al* [45] approximated $A(\boldsymbol{q})$ as

$$A(\boldsymbol{q}) = \frac{e^2\lambda^2}{\varepsilon c(1+q^2\lambda^2)} \quad (32)$$

where $\boldsymbol{q}^2 = |\boldsymbol{k}'_\perp - \boldsymbol{k}_\perp|^2$. The final expression of the scattering rate for electrons of wavevector $\boldsymbol{k}$ is

$$P^{dis}_{\nu\nu'}(\boldsymbol{k}_\perp,k_z,\Omega_{\boldsymbol{k}'_\perp,k_z}) = \frac{2\pi}{\hbar}\frac{n_{dis}e^4\lambda^4f^2}{\varepsilon^2c^2(1+q^2\lambda^2)^2} \times |I(\nu,\nu';\boldsymbol{k}_\perp,k_z,\boldsymbol{k}'_\perp,k_z)|^2 D_\perp(E',\Omega_{\boldsymbol{k}'_\perp,k_z}) \quad (33)$$

where n_{dis} is the density of the dislocation and $D_\perp(E',\Omega_{\boldsymbol{k}'_\perp,k_z})$ is the 2D density of states perpendicular to the $z(c)$ axis. Note that k_z is conserved after scattering since the dislocation scattering is two-dimensional.

The rate of electron scattering due to ionized impurities is calculated based on the Brooks–Herring (BH) approach [46], here modified for Bloch states. Within the BH formalism, the carrier is assumed to interact with a single ionized impurity and the screening parameter is used to account for many-body effects. If the distance between the scattering centers is smaller than the screening length, i.e. high doping density or low temperature, this screening procedure fails to represent the real scattering and the scattering needs to be treated as a two-body problem. This limitation is modified in Ridley's model by taking into account the probability of a particular ionized impurity being the nearest scattering center [47], which we use in the full band EMC simulations discussed in section 6.

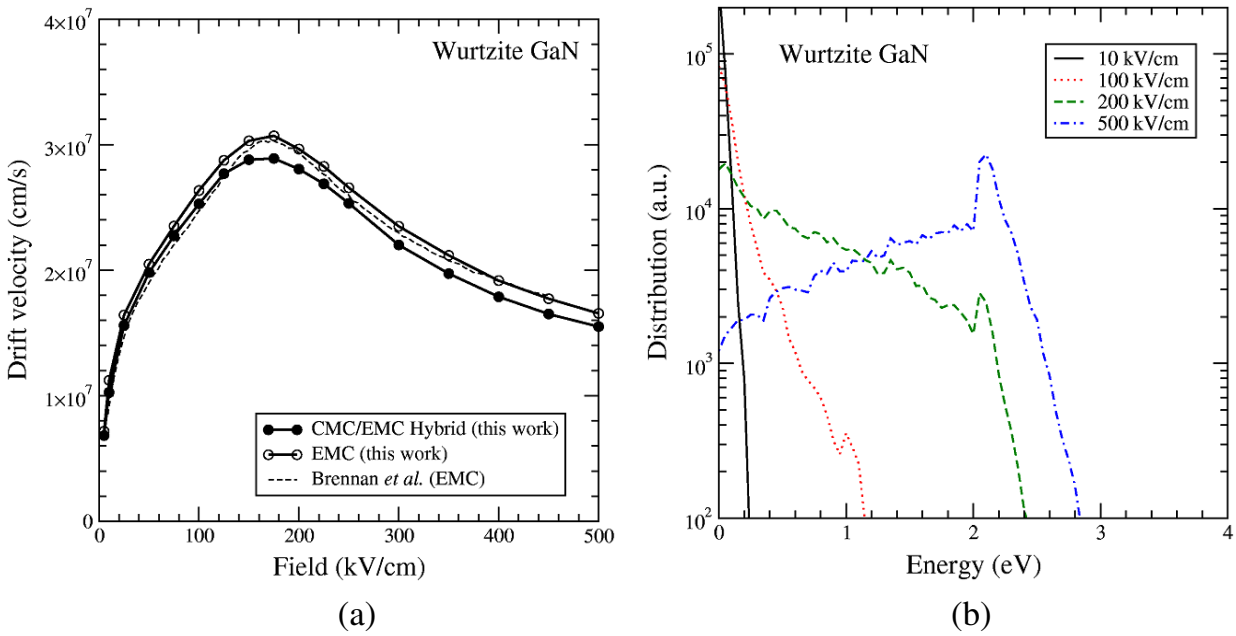

Figure 11. Calculated drift velocity and energy distribution at the various applied fields for wurtzite GaN at 300 K, assuming a constant deformation potential. (a) Electrical field versus drift velocity along the $(2\bar{1}10)$ direction; (b) energy distribution at the various fields.

6. Full band cellular Monte Carlo simulation

A full band cellular Monte Carlo (CMC) method is used to calculate the transport properties, in which the scattering rates for every initial and final state are tabulated over the Brillouin zone [48]. Since the CMC method pre-tabulates the scattering rates for every initial and final wavevector throughout the BZ, the determination of the final state after scattering is eliminated, which is typically computationally intensive in traditional full band EMC simulation. The trade-off is that a large amount of memory is needed to store the lookup table, typically several GBs. For that reason, we typically employ a hybrid simulator, where the CMC algorithm is used at lower energies where frequent scattering occurs, while a full band EMC simulation algorithm is used at high energies to minimize the amount of memory used. Another issue for the CMC algorithm is the accuracy of the final state energy, since it is only known within the uncertainty of the energy spanned by a given cell in k-space, whereas in EMC the final energy is determined exactly. This energy uncertainty error in the CMC is minimized by proper optimization of the grid size, where a nonuniform mesh in k-space is used to improve the accuracy in critical regions relative to transport, such as the conduction band minimum.

6.1. Velocity–field characteristics and distribution function

The transport properties of bulk zinc-blende and wurtzite GaN are first calculated and compared assuming a constant, isotropic, deformation potential. In this calculation, only phonon scattering, such as the deformation potential scattering and the polar optical phonon scattering, are taken into account. The electric field is applied along the $(2\bar{1}\bar{1}0)$ direction within the basal plane for wurtzite GaN and the (100) direction for zinc-blende GaN. In the case of wurtzite GaN, the CMC/EMC hybrid model is used in order to reduce the scattering table size since the IW size of wurtzite is about four times larger than zinc-blende. The EMC model is used when the electron energy is 3 eV above the bottom of the conduction band. Four conduction bands are taken into account for each calculation. The acoustic deformation potential is set as 10.1 eV, which is the same value used in the previous full band EMC calculation of wurtzite GaN by Brennan *et al* [17]. The non-polar optical phonon deformation potential of 13.2×10^8 eV cm^{-1} is used, which is obtained by the rigid pseudo-ion calculation in zinc-blende GaN discussed in section 3. A $76 \times 72 \times 40$ inhomogeneous grid is used for the first conduction band and a $50 \times 50 \times 20$ grid for the other bands in the calculation of wurtzite GaN. In the case of zinc-blende GaN, a $70 \times 70 \times 70$ inhomogeneous grid for the first conduction band and a $50 \times 50 \times 50$ grid for the other bands are used. The total required memory sizes for the transport calculation are 1.1 GB and 1.3 GB for wurtzite and zinc-blende, respectively.

Figures 11 and 12 show the applied field dependence of the drift velocity and the associated particle distribution functions for wurtzite and zinc-blende GaN. The previous results reported by Brennan *et al* [17] are also shown in the figures. Here a comparison is made between the CMC and a full band EMC simulation where the final state is chosen after scattering within the BZ. The results of CMC show good agreement with the results of EMC for both lattice structures, which suggests that energy uncertainty errors associated with the CMC are minimal.

The distribution of particles in the first BZ is shown in figure 13 for both wurtzite and zinc-blende. At low electric fields (100 kV cm^{-1} and below) the electrons are only in the Γ valley. As the electric field increases, the electrons begin to populate the second valley, which is at the U point for wurtzite

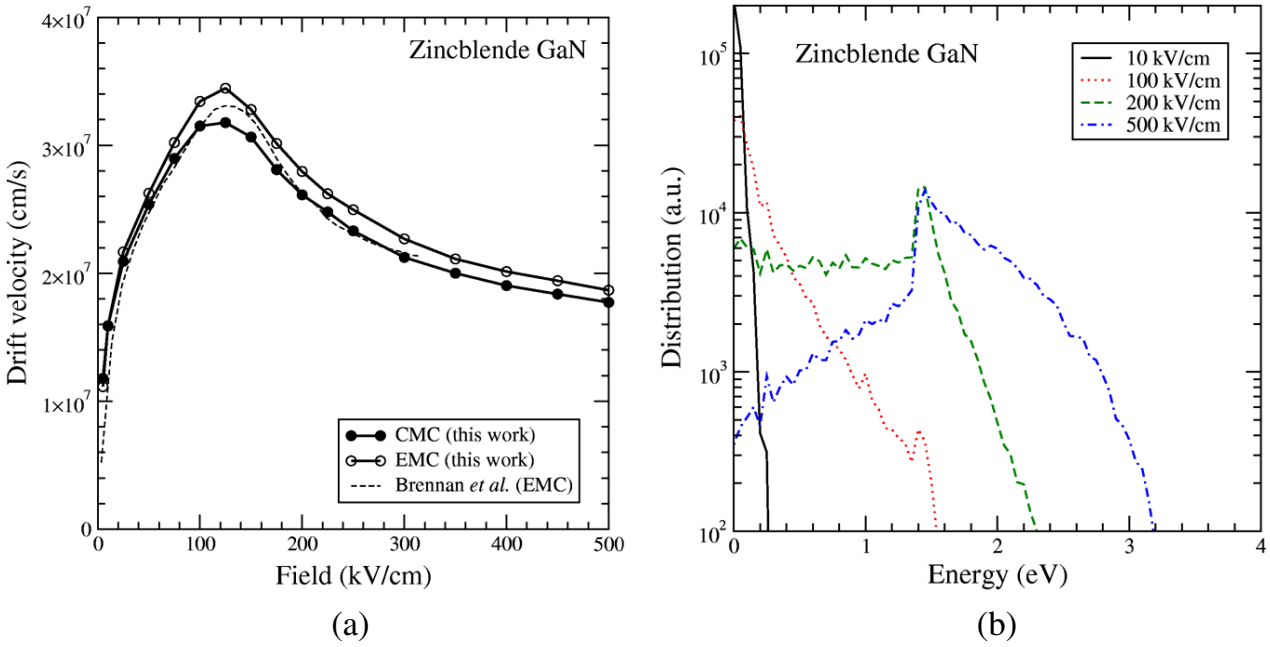

Figure 12. Calculated drift velocity and energy distribution at the various applied fields for zinc-blende GaN at 300 K, assuming a constant deformation potential. (a) Electrical field versus drift velocity along the (100) direction; (b) energy distribution at the various fields.

and the X point for zinc-blende. At extremely high electric fields, the electrons are distributed throughout the entire BZ for both lattice phases of GaN.

Figure 14(a) shows the simulated velocity–field characteristics for bulk GaN at 300 K based on the rigid ion model, compared with the constant deformation potential model, and with the experimental data of Barker *et al* [8]. As can be seen, the RIM model gives a systematically lower electron velocity compared with earlier constant deformation potential models. In comparison with experiment, with only deformation potential and polar optical phonon scattering included, the velocity–field characteristics are too high compared to experiment at low density, as shown in figure 14(b), while giving reasonably good agreement with the peak velocity measured above 200 kV cm^{-1}. While the peak velocity is mainly determined by phonon scattering (deformation, piezo- and polar-mode scattering), the low field region is primarily dominated by elastic mechanisms, including ionized impurity and dislocations. Here, an impurity density of 1.35×10^{17} cm^{-3} is used, which is taken from experimental data [8]. The dislocation density 3×10^9 cm^{-2} and charge fraction 0.5 are chosen to fit the experimental low field mobility data. The velocity with only impurity scattering or with impurity and piezoelectric scatterings is still higher than experimental data in the low electric field region. Including dislocation scatterings decreases the low field velocity and the simulated data show a good agreement with the experimental data. On the other hand, the constant deformation potential model cannot represent the experimental data even when these three scatterings are included, due to the higher peak velocity.

Figure 15 shows the field dependence of the drift velocity when the electric field is applied along the different directions. The $(2\bar{1}\bar{1}0)$ and $(10\bar{1}0)$ directions are within the basal plane. The peak velocities are slightly different but almost the same, especially in the high field region. This result shows that the anisotropic effects in the deformation potential do not play a significant role in terms of the velocity–field relationship in the different applied field directions.

In order to check the effect of the phonon model used, the velocity–field curve using the valence force model is compared with the phonon dispersion and eigenvectors calculated using the Keating model. As shown in figure 16, the velocity–field characteristics with the valence force model are nearly identical to the ones calculated using the Keating model. This shows that differences of the phonon model have only small effects on the transport characteristics.

Figure 17 compares the transient overshoot velocity calculated in GaN for both the constant deformation potential model and the full rigid ion model. As expected, the overshoot is less in the RIM case due to the higher net scattering and the corresponding reduction in velocity. Even in the RIM case, however, overshoot velocities in excess of 5×10^7 cm s^{-1} are predicted.

6.2. Nonequilibrium phonons

Under high electric fields, the emission of phonons drives the phonon distribution out of equilibrium and increases the net scattering rate, causing a reduction in velocity. Because of the high electric field and the high electron density in devices such as AlGaN/GaN HEMTs, nonequilibrium phonons may therefore play an important role in the transport properties. Recently, Ardaravičius *et al* [49] have shown the potential importance of nonequilibrium hot phonons in GaN high field transport. Here we include the effect on the LO optical phonon scattering. A rate equation approach is used, in which the dynamical evolution of the LO phonon distribution, N_q, can be described using a detailed balance of emission and absorption

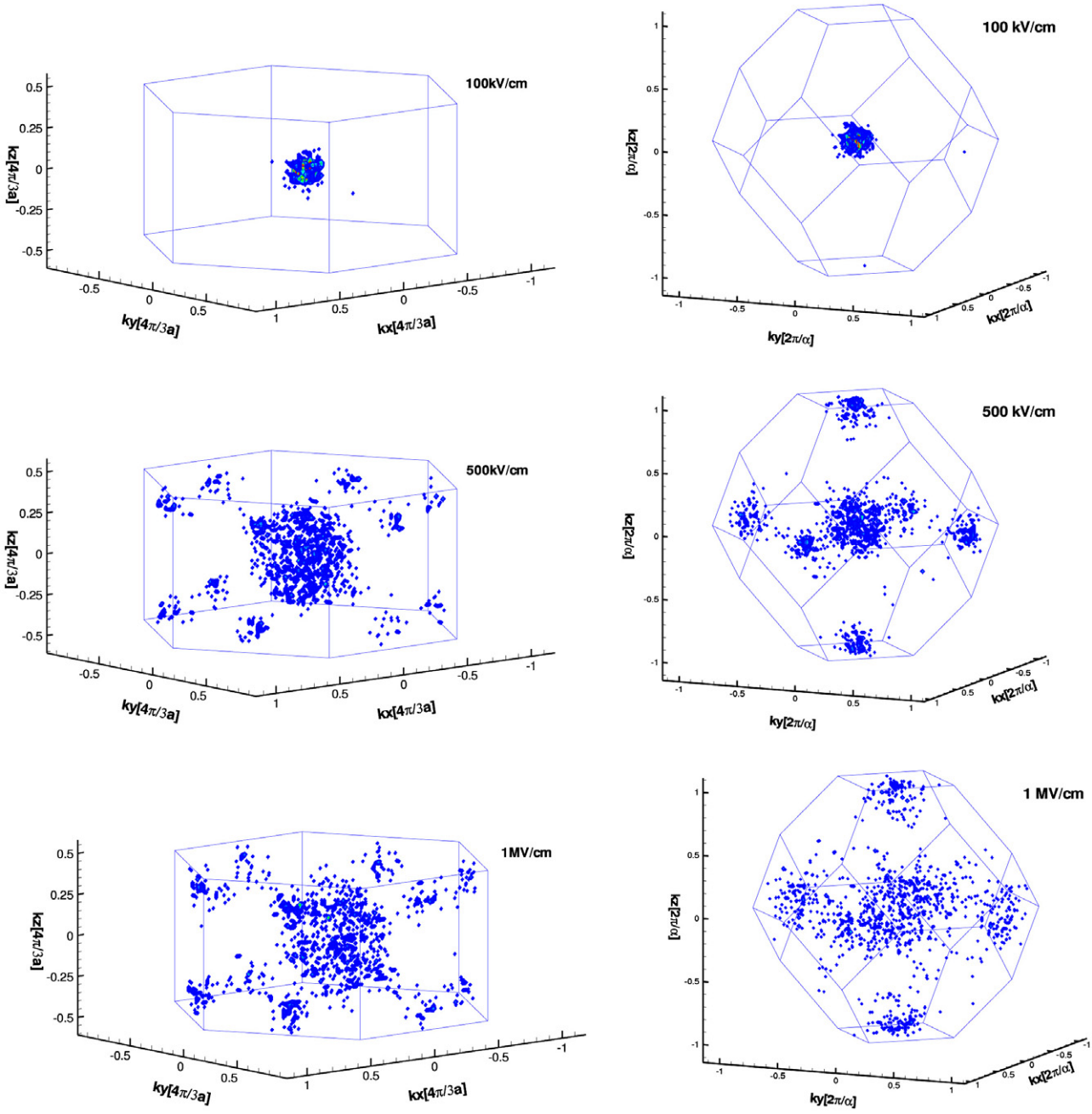

Figure 13. Carrier distribution in the first BZ for wurtzite (left) and zinc-blende (right) GaN at various electric fields.

events with the electron system, as well as the anharmonic decay of optical phonons into acoustic phonons [50]:

$$\frac{\partial N_q}{\partial t} = \left.\frac{\partial N_q}{\partial t}\right|_{\text{ph}-\text{c}} + \left.\frac{\partial N_q}{\partial t}\right|_{\text{ph}-\text{ph}};$$
$$\left.\frac{\partial N_q}{\partial t}\right|_{\text{ph}-\text{ph}} = -\frac{N_q - N_{\text{L}}}{\tau_{\text{op}}}. \tag{34}$$

The second expression represents the decay of the optical modes, characterized by the phonon relaxation time, τ_{op}. This value has recently been measured using time-resolved Raman scattering, where it is found to be a strong function of density decreasing in time as the density increases [51].

We have included hot phonons within the full band simulator in which k-space is discretized, and a phonon distribution, N_q, and a histogram, h_q, are defined over a grid in the k-space. At each time step of the simulation, the phonon distribution at $T = n\Delta t$ is calculated as

$$N_q(n\Delta t) = N_q((n-1)\Delta t) + \delta N_q(n\Delta t)\big|_{\text{ph-c}} - [N_q(n\Delta t) - N_{\text{L}}]\frac{\Delta t}{\tau_{\text{op}}} \tag{35}$$

where the first term on the rhs is the change in N_q due to scattering events with electrons (emission or absorption) and the second term is the decay of the phonon population over each time step due to phonon relaxation. Here a phonon

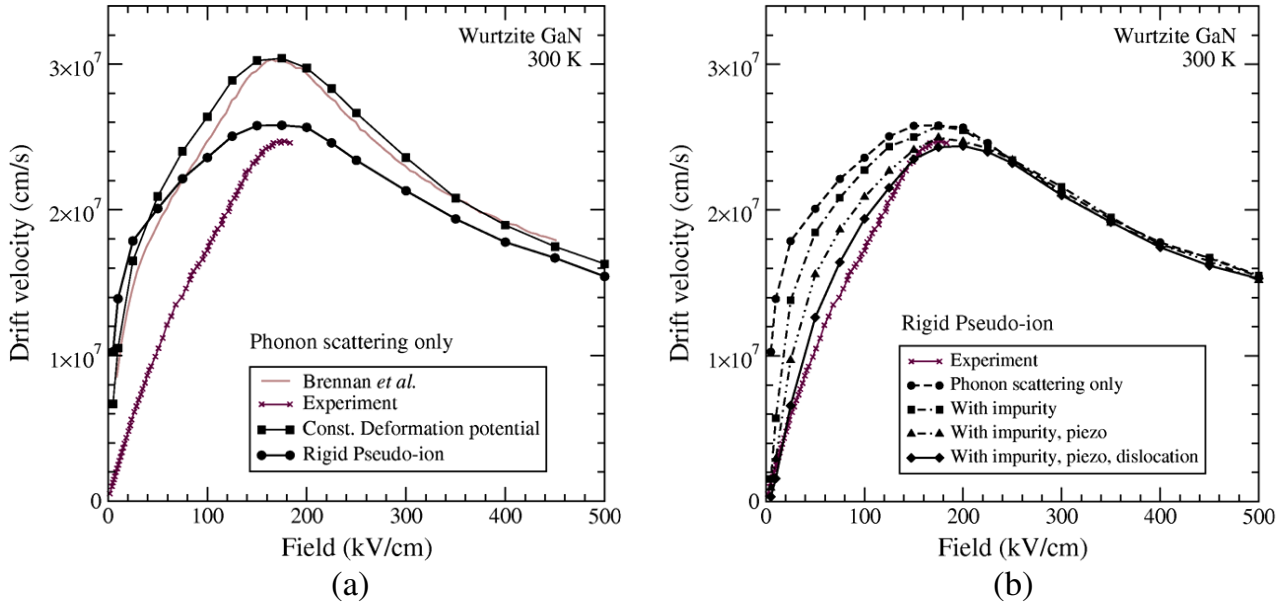

Figure 14. (a) Calculated velocity–field characteristics comparing the rigid pseudo-ion model, constant deformation potential, and the experimental results of Barker *et al* [8] and (b) calculated velocity–field characteristics including various scattering mechanisms based on the fully anisotropic rigid pseudo-ion model compared with experiment.

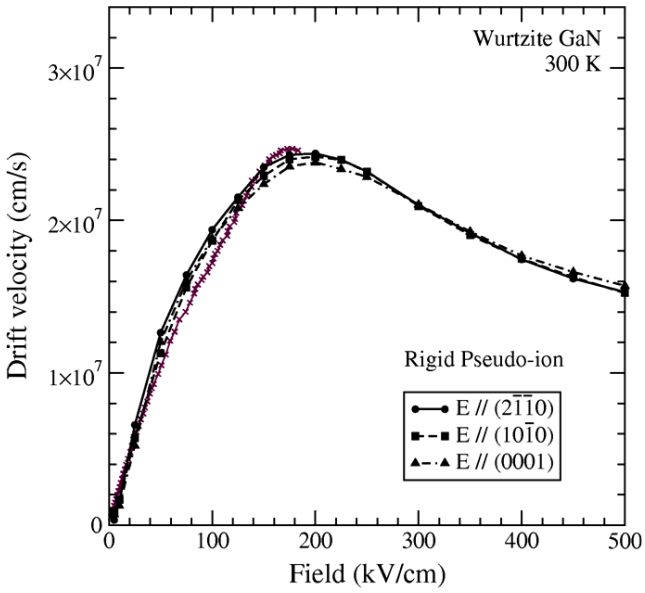

Figure 15. The velocity–field relationship for different field directions. The deformation potential scattering is calculated using the rigid pseudo-ion model. Impurity, piezoelectric and dislocation scatterings are included as well.

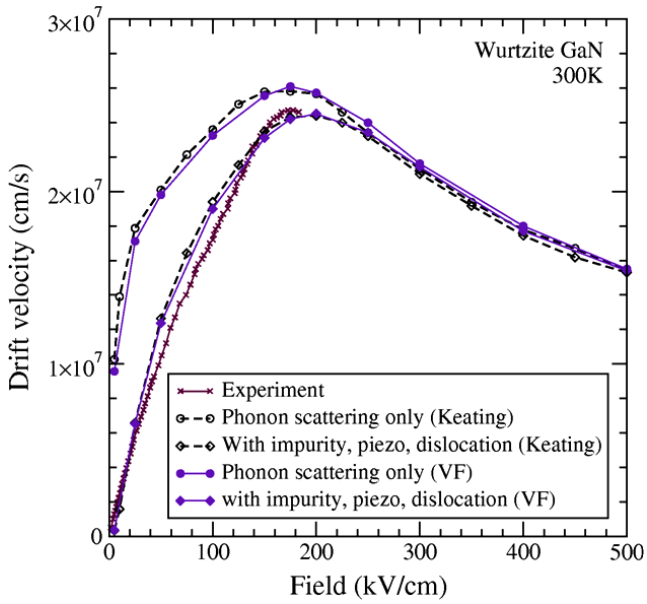

Figure 16. Velocity–field relationship using the Keating model and the valence force (VF) model in phonon calculations.

lifetime of 0.3 ps is assumed, corresponding to the higher density limit measured by Raman scattering [51]. Due to the temporally varying scattering rates, the CMC algorithm itself cannot be used, and rather a conventional full band EMC algorithm is used, using a self-scattering algorithm for the phonons [50]. The calculated effect on the velocity–field characteristics are shown in figure 18. As can be seen, at high carrier densities, a strong suppression of the carrier velocity due to the higher scattering rate associated with hot phonons occurs. Such effects may have a profound influence on device behavior, particularly AlGaN/GaN HEMTs, due to the high carrier density in the channel, which degrades the velocity, and hence the frequency response associated with the carrier transit time.

7. Conclusions

Herein we have presented a systematic study of the scattering rates and high field transport properties of wurtzite and

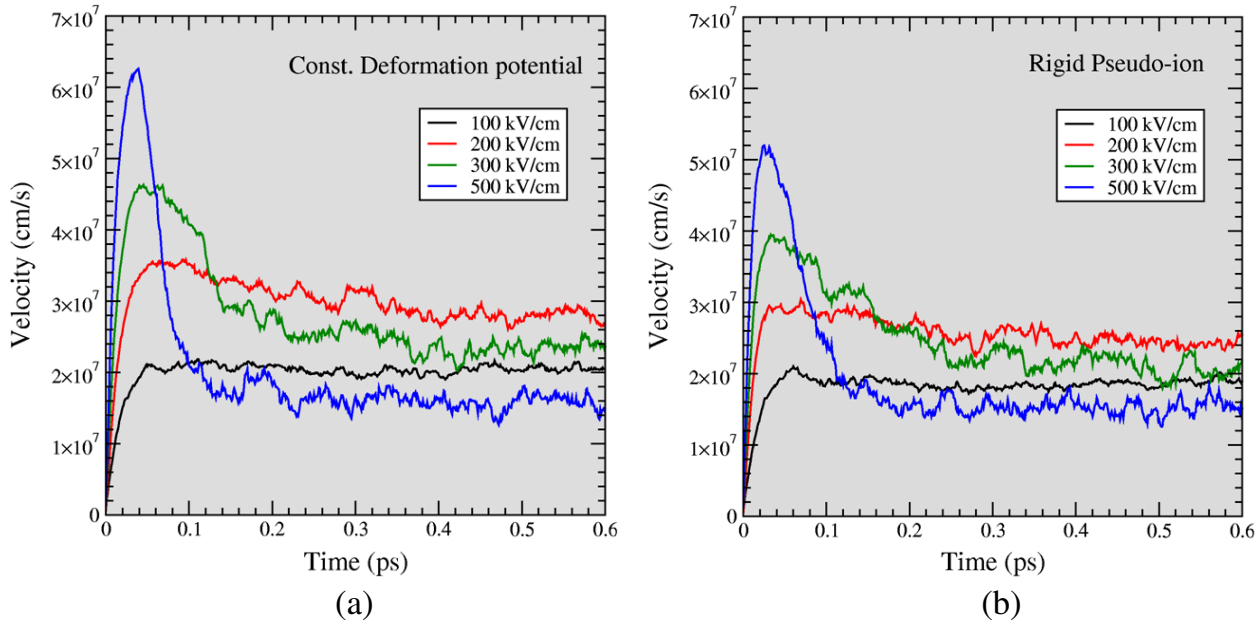

Figure 17. Velocity versus time for various electric field strengths for (a) the constant deformation model and (b) the rigid ion model.

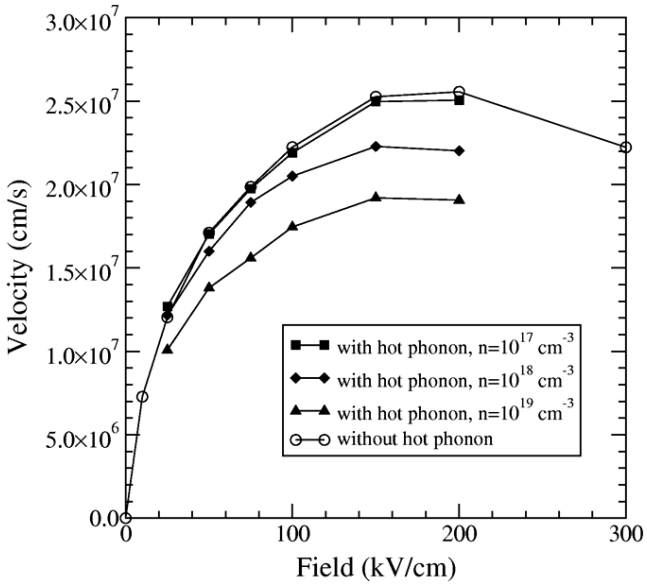

Figure 18. Calculated velocity–field characteristics including nonequilibrium hot phonons for several different bulk densities.

zinc-blende GaN using a microscopic rigid pseudo-ion method. We first show the relative sensitivity of the calculated scattering rates to the electronic band structure and lattice dynamics calculation, where it is shown that the RIM rates are relatively insensitive to the model chosen. The velocity–field characteristics were calculated including various scattering mechanisms including the RIM phonon scattering, and compared to pulsed I–V measurements in bulk material. It is found that, while the peak velocity is controlled primarily by deformation potential scattering (corresponding to the onset of intervalley scattering), at low fields dislocation and ionized impurity scattering dominate the experimental data. It is shown that there is very little anisotropy in the calculated velocity–field characteristics depending on the direction of the applied electric field, both in and out of the basal plane of the wurtzite phase. Finally, we investigated the effects of nonequilibrium hot phonons on the transport characteristics, where at high carrier density significant degradation of the peak velocity can occur.

Acknowledgments

The authors acknowledge the support of the National Science Foundation Grant ECS-0115548 and the Arizona Institute of Nanoelectronics.

References

[1] Nakamura S, Mukai T and Senoh M 1994 Candela-class high-brightness InGaN/AlGaN double-heterostructure blue-light-emitting diodes *Appl. Phys. Lett.* **64** 1687–9
[2] Chow T P and Tyagi R 1994 Wide bandgap compound semiconductors for superior high-voltage unipolar power devices *IEEE Trans. Electron Devices* **41** 1481–3
[3] Pearton S J, Ren F, Zhang A P and Lee K P 2000 Fabrication and performance of GaN electronic devices *Mater. Sci. Eng.* R **30** 55–212
[4] Ibbetson J P, Fini P T, Ness K D, DenBaars S P, Speck J S and Mishra U K 2000 Polarization effects, surface states, and the source of electrons in AlGaN/GaN heterostructure field effect transistors *Appl. Phys. Lett.* **77** 250–2
[5] Palacios T, Chakraborty A, Heikman S, Keller S, DenBaars S P and Mishra U K 2006 AlGaN/GaN high electron mobility transistors with InGaN back-barriers *IEEE Electron Device Lett.* **27** 13–5
[6] Higashiwaki M, Onojima N, Matsui T and Mimura T 2006 High f_T and f_{max} AlGaN/GaN HFETs achieved by using thin and high-Al-composition AlGaN barrier layers and Cat-CVD SiN passivation *Phys. Status Solidi* a **203** 1851–5

[7] Wraback M 2000 Time-resolved electroabsorption measurement of the electron velocity–field characteristic in GaN *Appl. Phys. Lett.* **76** 1155–7

[8] Barker J M, Akis R, Ferry D K, Goodnick S M, Thornton T J, Koleske D D, Wickenden A E and Henry R L 2002 High-field transport studies of GaN *Physica* B **314** 39–41

[9] Barker J M, Ferry D K, Goodnick S M, Koleske D D, Wickenden A E and Henry R L 2002 Measurements of the velocity–field characteristic in AlGaN/GaN heterostructures *Microelectron. Eng.* **63** 193–7

[10] Jacoboni C and Lugli P 1989 *The Monte Carlo Method for Semiconductor Device Simulation* (Vienna: Springer)

[11] Hess K 1991 *Monte Carlo Device Simulation: Full Band and Beyond* (Boston, MA: Kluwer Academic)

[12] Littlejohn M A, Hauser J R and Glisson T H 1975 Monte Carlo calculation of the velocity–field relationship for gallium nitride *Appl. Phys. Lett.* **26** 625–7

[13] Gelmont B, Kim K W and Shur M 1993 Monte Carlo simulation of electron transport in gallium nitride *J. Appl. Phys.* **74** 1818–21

[14] Mansour N S, Kim K W and Littlejohn M A 1994 Theoretical study of electron transport in gallium nitride *J. Appl. Phys.* **77** 2834–6

[15] Bhapkar U V and Shur M S 1997 Monte Carlo calculation of velocity–field characteristics of wurtzite GaN *J. Appl. Phys.* **82** 1649–55

[16] Kolník J, Oğuzman Í H, Brennan K, Wang R, Ruden P P and Wang Y 1995 Electronic transport studies of bulk zincblende and wurtzite phases of GaN based on an ensemble Monte Carlo calculation including a full zone band structure *J. Appl. Phys.* **78** 1033–8

[17] Brennan K F, Bellotti E, Farahmand M, Haralson J, Ruden P P, Albrecht J D and Sutandi A 2000 Materials theory based modeling of wide band gap semiconductors: from basic properties to devices *Solid-State Electron.* **44** 195–204

[18] Zollner S, Gopalan S and Cardona M 1989 Intervalley deformation potentials and scattering rates in zinc blende semiconductors *Appl. Phys. Lett.* **54** 614–6

[19] Kunikiyo T, Takenaka M, Kamakura Y, Yamaji M, Mizuno H, Morifuji M, Taniguchi K and Hamaguchi C 1994 A Monte Carlo simulation of anisotropic electron transport in silicon including full band structure and anisotropic impact-ionization model *J. Appl. Phys.* **75** 297–312

[20] Fischetti M V and Laux S E 1988 Monte Carlo analysis of electron transport in small semiconductor devices including band-structure and space–charge effects *Phys. Rev.* B **38** 9721–45

[21] Cohen M L and Chelikowsky J R 1988 *Electronic Structure and Optical Properties of Semiconductors* (Berlin: Springer)

[22] Oğuzman Í H, Kolník J, Brennan K F, Wang R, Fang T and Ruden P P 1996 Hole transport properties of bulk zinc-blende and wurtzite phase of GaN based on an ensemble Monte Carlo calculation including a full zone band structure *J. Appl. Phys.* **80** 4429–36

[23] Xia J-B, Cheah K W, Wang X-L, Sun D-Z and Kong M-Y 1999 *Phys. Rev.* B **59** 10119

[24] Schlüter M, Chelikowsky J R, Louie S G and Cohen M L 1975 *Phys. Rev.* B **12** 4200

[25] Bednarek S and Rössler U 1984 Calculation of the gamma–delta electron–phonon and hole–phonon scattering matrix elements in silicon *Phys. Rev. Lett.* **48** 1296

[26] Fischetti M V and Higman J M 1991 *Monte Carlo Device Simulation: Full Band and Beyond* (Dordrecht: Kluwer Academic) p 123

[27] Kunc K and Nielson O H 1979 Lattice dynamics of zinc-blende structure compounds using deformation-dipole model and rigid ion model *Comput. Phys. Commun.* **17** 413

[28] Azuhata T, Sota T, Suzuki K and Nakamura S 1995 *J. Phys.: Condens. Matter* **7** L129

[29] Zi J, Wan X, Wei G, Zhang K and Xi X 1996 Lattice dynamics of zinc-blende GaN and AlN: I. Bulk phonons *J. Phys.: Condens. Matter* **8** 6323

[30] Karch K, Wagner J-M and Bechstedt F 1998 *Phys. Rev.* B **57** 7043

[31] Fischetti M 1991 *Monte Carlo Device Simulation: Full Band and Beyond* ed K Hess (Boston, MA: Kluwer)

[32] Siegle H, Kaczmarczyk G, Filippidis L, Litvinchuk A P, Hoffmann A and Thomsen C 1997 Zone-boundary phonons in hexagonal and cubic GaN *Phys. Rev.* B **55** 7000–4

[33] Corczyca I, Christensen N E, Peltzer y Blancá E L and Rodriguez C O 1995 Optical phonon modes in GaN and AlN *Phys. Rev.* B **51** 11936–9

[34] Ruf T, Serrano J and Cardona M 2001 Phonon dispersion curves in wurtzite-structure GaN determined by inelastic x-ray scattering *Phys. Rev. Lett.* **86** 906–9

[35] Bulutay C, Ridly B K and Zakhleniuk N A 2000 Full-band polar optical phonon scattering analysis and negative differential conductivity in wurtzite GaN *Phys. Rev.* B **62** 15754–63

[36] Lee B C, Kim K W, Dutta M and Stroscio M A 1997 Electron–optical-phonon scattering in wurtzite crystals *Phys. Rev.* B **56** 997–1000

[37] Hamaguchi C 2001 *Basic Semiconductor Physics* (New York: Springer)

[38] Ridley B K 1999 *Quantum Processes in Semiconductors* 4th edn (Oxford: Oxford Science Publications)

[39] Chin V W L, Tansley T L and Osotchan T 1994 Electron mobilities in gallium, indium, and aluminum nitrides *J. Appl. Phys.* **75** 7365–72

[40] Wright A F and Furthmuller J 1998 Theoretical investigation of edge dislocations in AlN *Appl. Phys. Lett.* **72** 3467–9

[41] Wright A F and Grossner U 1998 The effect of doping and growth stoichiometry on the core structure of a threading edge dislocation in GaN *Appl. Phys. Lett.* **73** 2751–3

[42] Bonch-Bruevich V L and Glasko V B 1961 The theory of electron states connected with dislocations, I. Linear dislocations *Fiz. Tverd. Tela* **3** 36
Bonch-Bruevich V L and Glasko V B 1961 *Sov. Phys.—Solid State* **3** 26 (Engl. Transl.)

[43] Pödör B 1966 Electron mobility in plastically deformed germanium *Phys. Status Solidi* **16** K167

[44] Weimann N G, Eastman L F, Doppalapudi D, Ng H M and Moustakas T D 1998 Scattering of electrons at threading dislocations in GaN *J. Appl. Phys.* **83** 3656–9

[45] Look D C and Sizelove J R 1999 Dislocation scattering in GaN *Phys. Rev. Lett.* **82** 1237–40

[46] Brooks H and Herring C 1951 Scattering by ionized impurities in semiconductors *Phys. Rev.* **83** 879

[47] Ridley B K 1977 Reconciliation of the Conwell–Weisskopf and Brooks–Herring formulae for charged-impurity scattering in semiconductors: third-body interference *J. Phys. C: Solid State Phys.* **10** 1589

[48] Saraniti M and Goodnick S M 2000 Hybrid fullband cellular automaton/Monte Carlo approach for fast simulation of charge transport in semiconductors *IEEE Trans. Electron Devices* **47** 1909–6

[49] Ardaravičius L, Matulionis A, Liberis J, Kiprijanovic O, Ramonas M, Eastman L F, Shealy J R and Vertiatchikh A 2003 Electron drift velocity in AlGaN/GaN channel at high electric fields *Appl. Phys. Lett.* **83** 4038–40

[50] Lugli P, Bordone P, Reggiani L, Rieger M, Kocever P and Goodnick S M 1989 Monte Carlo studies of nonequilibrium phonon effects in polar semiconductors and quantum wells. I. Laser photoexcitation *Phys. Rev.* B **39** 7852–65

[51] Tsen K S, Kiang J G, Ferry D K and Morkoc H 2006 Subpicosecond time-resolved Raman studies of LO phonons in GaN: dependence on the injected carrier density *Appl. Phys. Lett.* **89** 112111